Nano Energy 84 (2021) 105905

Contents lists available at ScienceDirect

Nano Energy

journal homepage: http://www.elsevier.com/locate/nanoen

High performance (ZT>1) n-type oxide thermoelectric composites from earth abundant materials

Megha Acharya, Subhra Sourav Jana, Mani Ranjan, Tanmoy Maiti *

Plasmonics and Perovskites Laboratory, Department of Materials Science and Engineering, IIT Kanpur, U.P. 208016, India

ARTICLE INFO

Keywords:
Thermoelectrics
Oxide
Perovskite
Composite
Rare-earth-free

ABSTRACT

Oxide-based thermoelectric materials have the advantages of high-temperature stability, low toxicity and low processing cost comparted to other metal-based systems. However, achieving ZT > 1 remain elusive especially for n-type bulk oxide thermoelectrics. Here, we report the experimental demonstration of ZT > 1 in n-type oxides by synthesizing composites of Nb-doped $SrTiO_3$ (STN) with natural graphite. Introduction of conductive graphite inclusions in STN matrix has led to a surge in electrical conductivity due to 21-times increase in weighted mobility (μ_w) of electrons resulting in high thermoelectric power factor ~5400 $\frac{\mu W}{mK^2}$, which is ~16-times higher than that of pure STN. Furthermore, we could restrain the increase in thermal conductivity by attaining enhanced Umklapp scattering along with phonon-glass-like temperature-independent phonon mean-free-path above Debye temperature. We have achieved the maximum ZT ~1.42 in STN+ 0.5 wt% G composite, which is 15-times enhancement compared to STN. Our proposed way of designing rare-earth-free composites with graphite can potentially open up the possibility of fabricating novel high-temperature thermoelectric generators.

1. Introduction

The concept of scavenging the waste heat and converting it into electricity using thermoelectric generators (TEG) is being deliberated upon as a rewarding option, since less than 40% of the energy generated ends up being actually utilized with the rest released as waste heat [1,2]. Although, a TEG seems a very attractive option, its wide-scale commercialization has not been realized till date due to poor energy conversion efficiency as dictated by the figure of merit, $ZT = \frac{S^2\sigma T}{\kappa}$, where S = Seebeck coefficient, σ = Electrical conductivity, κ = Thermal conductivity with lattice (κ_l) and electronic (κ_e) contributors. It's a daunting task to design high-performance thermoelectric (TE) materials due to the interdependency of various constituent parameters in ZT. Moreover, conventional TE materials such as chalcogenides and intermetallics suffer from high processing cost, toxicity, limited operational temperature range, and chemical instability at high temperature. On the other hand, bulk oxides which can be rare-earth-free, economically feasible and stable at high temperature, have the potential to develop low-cost TEG for generating electricity from the enormous amount of waste heat produced in the manufacturing industries at temperatures above 900 K, hitherto remain untapped. However, bulk oxides suffer from poor ZT values compared to the metal-based systems. Although some p-type oxides such as oxychalcogenides [3], layered cobaltites [4,5] have shown promises, there is a dearth of highly efficient n-type TE bulk oxides at present. Recently, $SrTiO_3$ has emerged as a potential n-type oxide to show good TE properties by doping [6–10] with La, Nb and grain-size engineering [11]. Till date, the maximum ZT value reported for n-type bulk oxides is ~ 0.6 at 1100 K for 10% Nb and 10% La co-doped $SrTiO_3$ [8]. Designing composites [12–17] of TE materials with graphene has been proven to be one of the best strategies to troubleshoot the conundrum of decoupling $S^2\sigma$ and κ_l in order to enhance the ZT values.

Inspired by enhanced thermoelectric properties observed in composites of chalcogenides and skutterudites with graphene [12–14], Lin et al [15]. have used the same strategy in oxide thermoelectrics by incorporating graphene in La-doped $SrTiO_3$. They have achieved maximum ZT value of 0.42 at room-temperature for the composite with 0.6 wt% graphene, much higher than the ZT of the pure oxide. Similarly, researchers have been able to enhance the ZT (< 0.3) values of Nb-doped $SrTiO_3$ by fabricating composites with reduced graphene oxide [16,17]. Better thermoelectric performance in composites of doped-$SrTiO_3$ with graphene has been attributed to simultaneous increase in electrical conductivity as well as phonon scattering at oxygen vacancy sites, nanostructured grains and heterointerfaces of graphene with the oxide

* Corresponding author.
E-mail address: tmaiti@iitk.ac.in (T. Maiti).

https://doi.org/10.1016/j.nanoen.2021.105905
Received 21 November 2020; Received in revised form 3 February 2021; Accepted 16 February 2021
Available online 20 February 2021

grains [15]. In spite of all the efforts in the direction of oxide composites, achieving ZT > 1 for bulk n-type oxides seems far to reach at the moment. Hence, fresh approaches are warranted in selection and design of oxide-based thermoelectric materials. Incorporation of r-GO in Nb-doped $SrTiO_3$ has reduced the minimum lattice thermal conductivity from 3–4 W/m-K to 2–3 W/m-K [16,17]. When we compare the thermoelectric performance of the doped-$SrTiO_3$-based composites with state-of-the-art thermoelectrics like tellurides and selenides, it is apparent that in spite of making composites with graphene, thermal conductivity of these oxide-based thermoelectrics are much higher than that of the tellurides, which exhibit k less than 1 W/m- K [18,19]. Graphene which has a large thermal conductivity, ~ 3500 W/m- K [20] fails to lower the overall thermal conductivity of the composites significantly in spite of inducing interfacial phonon scattering at grain boundary. In this aspect, graphite, one of the cheapest electrically conductive materials offers an interesting choice as it exhibits much lower thermal conductivity especially along c-axis (2 W/m.K) [20] compared to graphene. However, no such reports on thermoelectric properties of graphite-based composites with oxides or chalcogenides have been found in the literature.

Herein, we report ZT > 1 in rare-earth-free oxide thermoelectrics by fabricating composites of 15 mol% Nb-doped $SrTiO_3$ (STN) with natural graphite (G), most stable allotrope of carbon, via fast sintering process called spark plasma sintering (SPS) as shown schematically in Fig. 1. We have achieved maximum ZT ~ 1.42 in STN + 0.5 wt% G composite, which is more than twice the highest ZT value ever reported in the literature for n-type bulk oxides [8]. Unlike 2D materials like graphene, which has been mostly found [15–17,21] to be segregated along the grain boundaries, incorporation of graphite in a perovskite oxide has led to the formation of nano-inclusions as well as large micron-size grains in the microstructure of oxide matrix. Interestingly, we have observed 21-times increase in weighted mobility (μ_w) of electrons due to incorporation of graphite in STN. As a result, we have attained an order of magnitude increase in electrical conductivity without imposing any significant detrimental effect on Seebeck coefficient values, leading to the large enhancement in thermoelectric power factor~ $5400\mu W/mK^2$ in the STN+G composite. Further, we have been able to suppress κ_l using grain-size engineering and reducing the phonon's mean-free path, causing more phonon-phonon scattering due to graphite inclusions in STN matrix. Especially at high temperatures, STN+G composites exhibit phonon glass-like thermal conductivity resulting in high ZT values. Our approach of using graphite among other carbon allotropes in the composites of oxides comprising earth-abundant elements thus opens up a new avenue for designing low-cost n-type bulk oxide thermoelectric materials.

2. Experimental

2.1. Synthesis of $SrTi_{0.85}Nb_{0.15}O_3$ graphite nanocomposites

The processing has been started with a stoichiometric batch of $SrTi_{0.85}Nb_{0.15}O_3$ (STN) using high purity precursor oxides and carbonates, i.e., $SrCO_3$ (99.99% purity, Sigma Aldrich), TiO_2 (99.99% purity, Sigma Aldrich) and Nb_2O_5 (99.99% purity, Sigma Aldrich) to fabricate the base oxide, STN. The powders have been vigorously mixed in the necessary molar ratio followed by milling with ZrO_2 balls as grinding media and ethanol as the solvent for 24–48 h at 300 rpm. After drying and crushing the mixture of powders, the same has been calcined at 1750–1850 K with a holding time of 15–16 h in reducing atmosphere for multiple (3−5) times to attain a single crystalline phase, as confirmed with X-Ray diffraction study. After establishing crystalline $SrTi_{0.85}Nb_{0.15}O_3$ as a single phase, the nanocomposite has been synthesized by adding desired weight-percentage of high-purity graphite powder (natural, briquetting grade, −100 mesh, 99.9995% purity, Alfa Aesar), which has been followed by homogenizing the composite powder by crushing in mortar and pestle. The attainment of nano-sized particles has been done by wet-milling using ethanol as solvent and ZrO_2 as grinding media at 600 rpm for 2–3 h in a planetary micro-mill (Fritsch, PULVERISETTE 7 premium line). The milled composite powders have been annealed in reducing atmosphere at 1250–1300 K with a soaking time of 2–3 h. The compaction of the powders to form highly dense pellets has been done using the spark plasma sintering technique at a temperature of 1700–1750 K with a holding time of 3–5 min, heating and cooling rate of 50 K/minute, under a pressure of 30–50 MPa in an inert atmosphere.

2.2. Characterization

In order to determine the thermoelectric parameters, i.e., Seebeck coefficient (S) and electrical conductivity (σ) of the composites, the dense pellets prepared by SPS have been characterized using the ZEM-3M10R, ULVAC-RICO Inc. apparatus in the temperature range from 300 K to 1123 K. Details of the thermoelectric measurement can be found in our earlier reports [22]. The sintered pellets have been characterized by a range of techniques like X-Ray diffraction (Rigaku Smartlab High-Resolution X-Ray Diffractometer), thermal diffusivity (Laser Flash System LFA 457, Netzsch) and specific heat measurement (DSC 204 F1 phoenix, Netzsch), nano-indentation (TI 750; Hysitron Ltd.), Raman spectroscopy (Acton series SP 2500i, Princeton instruments), FE-SEM, electron backscatter diffraction (JSM-7100 F, JEOL), X-Ray photoelectron spectroscopy (PHI 5000 Versa Probe II, FEI Inc.) and carrier concentration measurement (HMS-5000 Series Hall

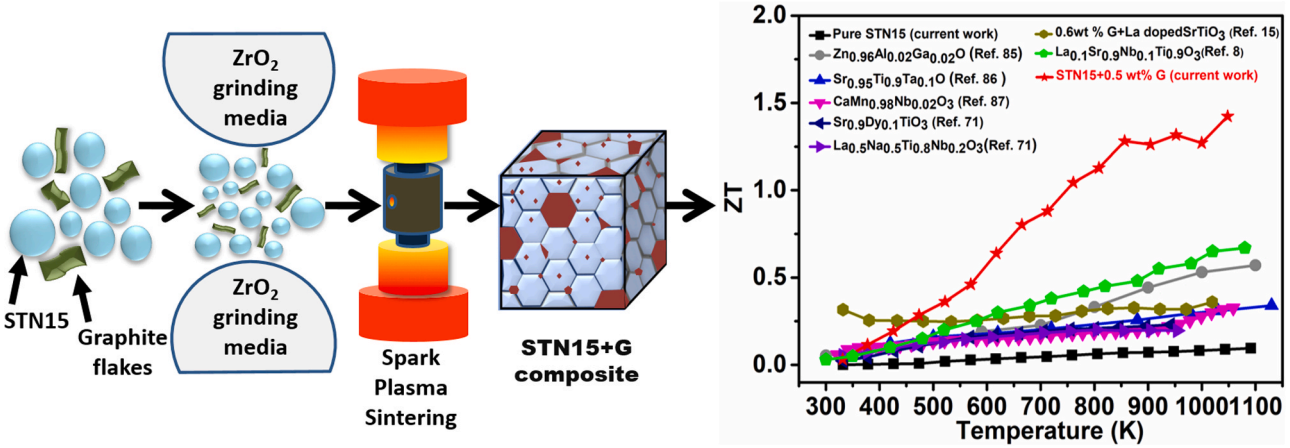

Fig. 1. Schematic representation on processing of bulk oxide composites of $SrTi_{0.85}Nb_{0.15}O_3$ matrix with graphite inclusions demonstrating record high ZT values compared to previously reported n-type oxides [8,15,71,85–87].

Effect measurement system, Ecopia) to gauge the behavior of the composites with variation in weight percentage of graphite for high temperature thermoelectric applications. The Raman spectroscopy measurements have been carried out at room temperature using a solid-state laser of wavelength 532 nm.

3. Results

3.1. Phase and microstructure analysis

The XRD analysis of all the SPS-sintered samples imply the existence of a single phase (cubic) of STN along with the signature of graphite peak at ~26.5° as shown in Fig. 2(a). It is evident from Fig. 2(b) that the intensity of the XRD peak corresponding to graphite becomes more prominent with the increase in graphite content in these composites, as expected. Further, we have evaluated the structural stability of these composites by high-temperature XRD analysis. It is imperative that these composites are stable in the entire temperature range of measurement, 303–973 K as the XRD profiles remain unchanged along with the retention of the graphite peak (Fig. S3), although the peak shifting due to thermal expansion has been observed, shown in Fig. 2(c).

The Raman spectra of all the sintered composites have corroborated the existence of carbon in the form of graphite. The spectra exhibit a minor peak at 1347 cm^{-1} and a sharp peak at 1581 cm^{-1} corresponding to D-band and G-band respectively as shown in Fig. 2(d). However, no such peak corresponding to 2D-band has been found around 2440 cm^{-1} Raman shift, although a prominent peak for 2 G-band has been identified in the Raman spectra as shown in Fig. S5. The small D-band has been observed due to the structural defects occurred upon mechanical exfoliation [23] of the graphite flakes during repeated milling cycles involved in the materials processing [24,25]. Further, to confirm the exfoliation, we have collected the Raman spectra for both pristine graphite as well as nanomilled graphite powder and observed the existence of a minor peak corresponding to the Raman shift for D-band in addition to the G-band (Fig. 2(d)) for nanomilled graphite. This has confirmed the retention of graphite in the unoxidized state validating our observations from the XRD analysis. It is to be noted that identical Raman spectra have not been obtained for all the locations of the sample observed under optical microscope as shown in Fig. S6. Raman spectra of the dark patches observed in the microscope image have shown distinct and sharp G-band Raman shift validating the presence of graphite inclusions. However, no such peak has been observed in the lighter zone (matrix) suggesting the presence of demarcated graphite islands in STN matrix. Further, to clarify the distribution of graphite in STN+G composites, microstructural analysis has been carried out using FE-SEM. The white spots depicting the distribution of nano-scale graphite as inclusions in the microstructure, shown in Fig. 2(e), have been found to be carbon-rich in the EDS spot spectra analysis (Table S2 and Fig. S7). Although FE-SEM image suggests the nano-scale inclusions of graphite in STN matrix, we have also observed large micron-sized graphite inclusions as comparable with STN grains in the Electron Backscatter Diffraction (EBSD) band (Fig. 2(f)) and phase contrast

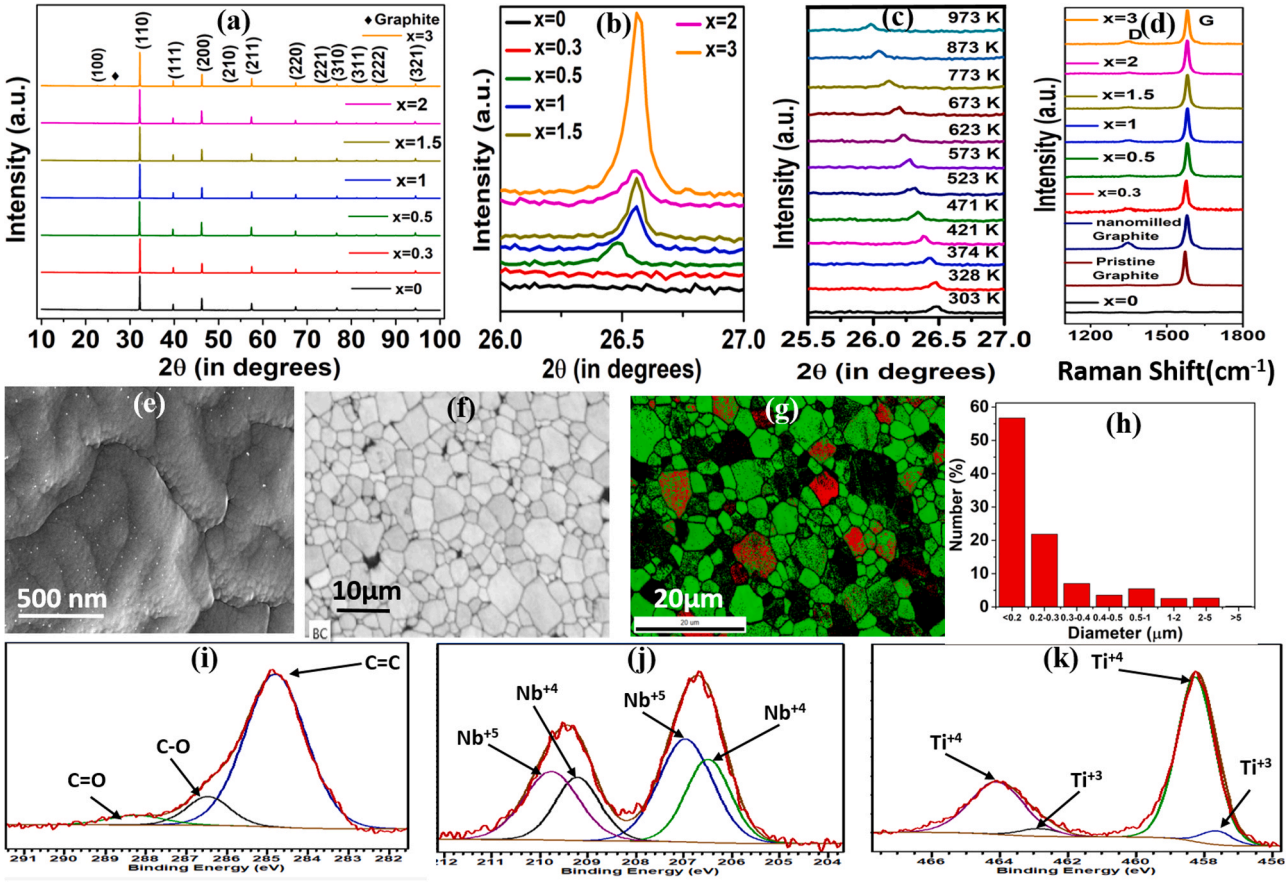

Fig. 2. Phase and microstructure analysis, (a) XRD plots for the sintered compositions of STN+x wt% G ($0 < x \leq 3$) (b) position of the XRD peak due to Graphite in the sintered composites STN+x wt% G ($0 < x \leq 3$) (c) High-temperature XRD plot for STN + 0.5 wt% G showing the peak of Graphite at $2\theta = 26.5°$ within 303–973 K (d) Raman Spectra for sintered composites, precursor Graphite powder (pristine graphite) and nano-milled graphite (e) FESEM microstructure for STN + 1.5 wt% G (f) Band contrast image and (g) Phase contrast image with the red-colored regions or pockets denoting Graphite and the green-colored regions representing STN, (h) Grain size distribution for the EBSD microstructure of STN + 0.5 wt% G and (i–k) XPS spectra for Carbon, Titanium and Niobium in STN + G composites, respectively.

images (Fig. 2(g)). Both FE-SEM and band contrast images have revealed a very dense microstructure with nm to μm-sized graphite inclusions embedded in the STN matrix. A wide grain size distribution consisting of 6–7% of the grains more than 1 μm in size and more than 50% of the grains below 200 nm has been attained for all the STN+G composites as evident from the bar chart (Figs. 2h and S8) calculated from the TSL-OIM analysis of EBSD patterns. Attainment of a wide grain size distribution can be attributed to the quick and effective densification through optimization of SPS parameters. It has been recently reported that bimodal grain size distribution due to abnormal grain growth in STN system is beneficial for enhancing thermoelectric power factor [11]. Although no such abnormal grain growth has been detected in the microstructure of STN+G composites, we have found the coarser grains surrounded by smaller grains without losing the connectivity between them, which can be instrumental in decoupling $S^2\sigma$ and κ_l. Nanoscale grains are known to facilitate phonon scattering resulting in reduced mean-free path of phonons and low thermal conductivity [26]. Larger microscale grains are likely to aid the transport of charge carriers in polycrystalline ceramics. It is to be noted here that unlike the earlier work on graphene-based composites [15–17] with STN where graphene or r-GO are segregated in the grain boundary of STN matrix, in the present work we have obtained the nanoscale inclusions of graphite along with micron-sized graphite grains distributed in the STN matrix.

The X-Ray photoelectron spectroscopy (XPS) analysis has revealed the presence of elemental carbon in the form of graphite as most of the carbon atoms have been found to exhibit C-C bond shown in Fig. 2(i) and Table S3. Additionally, traces of C=O and C-O bonds have been identified in the XPS spectra, which is expected to be due to the exfoliation of the graphite flakes during processing. Deconvolution of the XPS peaks of Nb and Ti has revealed that almost 60% of Nb is present as Nb^{5+} and rest as Nb^{4+}, although most of the Ti (93%) has been found in the form of Ti^{4+} (Fig. 2j–k and Table S3).

$$Nb_2O_5 \xrightarrow{SrTiO_3} 2Nb_{Ti}^{\cdot} + 2e' + 4O_O^{\times} + \frac{1}{2}O_2 \quad (1)$$

$$O_O^{\times} \rightarrow \frac{1}{2}O_2 + V_O^{\cdot\cdot} + 2e' \quad (2)$$

The presence of Nb^{5+} at Ti-site in $SrTiO_3$ has caused the creation of electrons, which can be explained through defect reaction (1). Besides, processing of STN powder in reducing atmosphere can produce inherent defects like oxygen vacancies in the oxides as per Eq. (2).

3.2. Thermoelectric transport

The dominant charge carriers in the STN+G composites have been found to be electrons, as evident from the negative Seebeck coefficient values obtained in the whole temperature range of measurement as shown in Fig. 3(a). However, thermopower values for all the compositions have been found to follow a common trend of monotonic increase in magnitude with temperature inferring a degenerate semiconductor-like behavior arising from the enhanced scattering of electrons at high temperature. It is to be noted that the incorporation of conductive graphite in STN matrix causes 20% decrease in room temperature Seebeck coefficient values from 75 $\mu V/K$ for pure (x = 0) STN sample to 60 $\mu V/K$ for 3 wt% G composite. Also, high temp (~1050 K) Seebeck value has been found to be decreased by 15% from 185 $\mu V/K$ for pure (x = 0) STN to 157 $\mu V/K$ for 3 wt% G composition.

However, the decrease in Seebeck coefficient is trivial compared to the order-of-magnitude increase in the electrical conductivity observed in STN due to graphite loading as evident in Fig. 3(b). For the room-temperature conductivity values, the surge is as high as 46-times i.e., from 4.4×10^3 S/m for STN to 2.1×10^5 S/m for the STN + 1 wt% G composite. The maximum value of electrical conductivity obtained is 3.2×10^5 S/m for STN + 1 wt% G, which accounts for ~ 21-times increase in the σ_{max} value of pure STN (1.5×10^4 S/m). It is to be noted that the maximum conductivity of STN itself has been improved by ~ 17-times compared to our earlier work [27] due to an additional heat-treatment step at 1300 K in reducing (H_2) atmosphere just before sintering and processing optimization resulting in a wide range of grain size distribution (nm to μm scale). Although, similar values of electrical conductivity on the order of 10^4 S/m have been reported in the literature for Nb-doped $SrTiO_3$ [8,9,11]. The surge in the electrical conductivity values for STN-graphite composites without significant impact on thermopower has contributed most effectively in enhancing the power

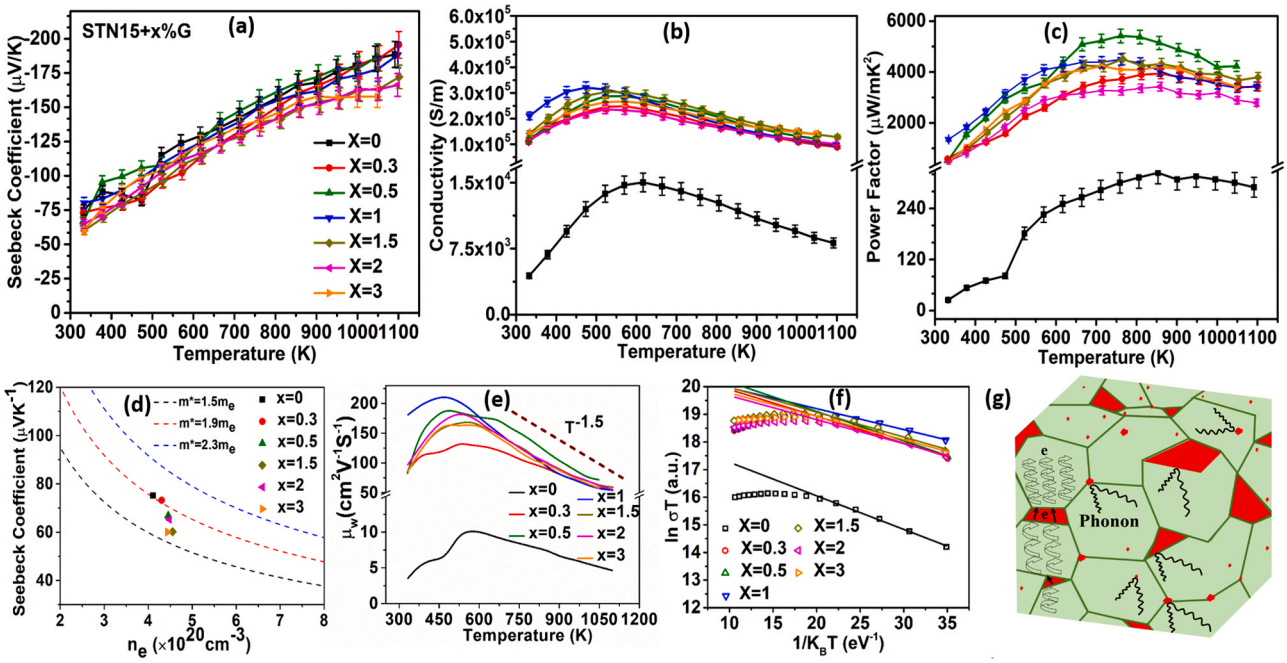

Fig. 3. Electrical properties: (a) Seebeck coefficient with Temperature (b) Electrical Conductivity with Temperature (c) Power factor ($S^2\sigma$) with Temperature (d) Pisarenko plot (e) Weighted mobility with Temperature (f) ln(σT) vs. $1/K_BT$ for the sintered STN+x wt% G composites ($0 \leq x \leq 3$) (g) Schematics of the electron hopping and phonon scattering by the graphite inclusions.

factor (Fig. 3(c)). The maximum power factor (PF) $\sim 5400\ \mu W/mK^2$ has been obtained in STN + 0.5 wt% G composite, which is 16-times more than that of pure STN ($\sim 320\ \mu W/mK^2$) and is by far the best result obtained in any n-type oxides including $SrTiO_3$-based perovskites [28–30]. Furthermore, we have checked the cyclability of these composites by collecting thermoelectric data in both heating and cooling cycles. It is evident from Fig. S11 that thermoelectric parameters do not show significant hysteresis in these composites.

Interestingly, we have found that introduction of graphite in the STN matrix doesn't affect its bandgap, which has been estimated for all the STN + G compositions to be within the range of 3.08–3.14 eV using Kubelka-Munk fitting of the diffused Reflectance (R_∞) data collected by UV–visible spectroscopy shown in Fig. S9 and Table S4. Furthermore, we have estimated the charge carrier concentration (n) for the composites at room-temperature using Hall measurement technique and found similar values for all the compositions ($(4.1 - 4.7) \times 10^{20}\ cm^{-3}$) as shown in Fig. S10. The effective mass (m*) has been estimated using the expression for Seebeck coefficient of the degenerate semiconductor $\left(S = \frac{8\pi^2 k_B^2}{3eh^2} m^* T \left(\frac{\pi}{3n}\right)^{2/3}\right)$ reported in the literature [7,31,32]. It is apparent from the Pisarenko plot shown in Fig. 3(d) that the effective mass of electron has been decreased due to graphite incorporation in STN matrix, dwelling in the range form 1.5–1.9 m_e. Similar values of effective mass have been found in the literature for STN-based materials [10,28]. For better understanding of electron-transport phenomena, weighted mobility (μ_w), which is independent of carrier concentration is posited [33–37] as a better descriptor as expressed by the following equation.

$$\mu_w = \mu_0 (m^*/m_e)^{3/2} \tag{3}$$

Where μ_0 is drift mobility. Weighted mobility (μ_w) for all the composite samples is calculated based on the Seebeck coefficient and electrical conductivity data, using the following expression [34],

$$\mu_w = \frac{3h^3\sigma}{8\pi e(2m_e k_B T)^{3/2}} \left[\frac{exp\left[\frac{|S|}{k_B/e} - 2\right]}{1 + exp\left[-5\left(\frac{|S|}{k_B/e} - 1\right)\right]} + \frac{\frac{3}{\pi^2}\frac{|S|}{k_B/e}}{1 + exp\left[5\left(\frac{|S|}{k_B/e} - 1\right)\right]} \right] \tag{4}$$

It can be seen from Fig. 3(e) that the weighted mobility at lower temperatures shows increasing trend suggesting thermally-activated charge transport before it decreases with temperature by $T^{-3/2}$ dependency above 500–600 K indicating metal-like electrical conductivity due to the scattering of electrons by acoustic phonons. Although the room-temperature weighted mobility for all the STN + G composites is slightly lower than single crystal STN, it begins to follow single crystal-like mobility with increasing temperature. The maximum weighted mobility $\sim 212\ cm^2V^{-1}S^{-1}$ has been obtained for 1 wt%G at 473 K, which is 21-times higher as compared to the pristine STN inferring single crystal-like behaviour due to graphite incorporation. Such high values of weighted mobility can be attributed to be the reason behind the order of magnitude increase in electrical conductivity resulting in the phenomenal rise in power factor obtained in these composites.

In order to understand the impact of using graphite on the enhancement of thermoelectric power factor in our oxide composites, results reported by the earlier researchers on doped-$SrTiO_3$-based composites are summarized in Table S5 in Supporting Information. It may appear odd that Seebeck coefficient of our STN+G composites has changed only 15–25% in spite of phenomenal increase in electrical conductivity. However, Okhay et al [17]. and Wang et al [38]. have also reported almost no change (< 5%) in Seebeck coefficient for the composites of STN with YSZ and r-GO, respectively in spite of order-of-magnitude increase in their electrical conductivity. What makes our current STN + G system interesting is that electrical conductivity has not decreased much at higher temperatures, securing more than 10^5 S/m in the whole temperature range from 300 to 1100 K. On the contrary, composites of STN with graphene (r-GO) or YSZ have shown an order-of-magnitude decrease in electrical conductivity at high temperatures giving rise to the conductivity values on the order of 10^4 S/m around 1100 K. At the outset, it is to be noted that all the previous efforts have dealt with graphene or r-GO which have been found to segregate in the grain boundary regions with the morphology of flakes or sheets. However, our STN + G samples comprise of graphite nano-inclusions which makes our system more similar to earlier report on STN with YSZ nanoinclusion system [38]. Besides, we have also obtained large micron-sized graphite grains distributed in STN matrix. Hence it is expected to affect the charge transport properties of perovskite oxides differently than graphene, which has been reported to facilitate the charge transport by reduction of Schottky barrier height in the grain boundaries, resulting in excess oxygen vacancies at the vicinity of grains of polycrystalline materials [39]. Although graphite is supposed to create a reducing atmosphere, it is expected to be different than the reducing environment created by r-GO modified grain boundaries of oxide ceramics. Moreover, the order-of-magnitude increase in weighted mobility, μ_w obtained in our composites cannot be attributed only to the oxygen vacancy formation like graphene-based composites [21,33,40] where, the grain-boundary refinement in polycrystalline materials by highly conductive 2D graphene enabled it to behave like single crystal. It is to be noted here that STN + G composites exhibit not much deterioration in Seebeck coefficient in spite of large enhancement in electrical conductivity unlike the earlier reports on composites of $SrTiO_3$ (STO) with rGO, where increase in conductivity was obtained at the expense of drastic fall in Seebeck coefficient due to manifold increase in carrier concentration [21,33,40]. Nevertheless, it can be concluded that the charge transport in STN+G composites is driven by electron mobility.

In order to understand the reasons behind an order-of-magnitude increase in electrical conductivity in spite of having similar carrier concentration, and bandgap, one needs to look more carefully at the temperature dependent conductivity curve shown in Fig. 3(b). STN+G composites have demonstrated semiconductor ($d\sigma/dT > 0$) to metal-like ($d\sigma/dT < 0$) transition (S-M) in the temperature range 470–620 K for all the compositions (Table S6 & Fig. S12). Although earlier studies have reported [17,38] no change in Seebeck coefficient values but observed the change in electrical conductivity behavior of STN from semiconductor to metallic nature by formation of composite with graphene or YSZ, not much explanation has been provided for such behavior. However, such interesting phenomena of S-M transitions called Mott transitions have been reported in a wide range of oxide materials including perovskites [41–44], when the Mott criteria (Eq. 5) is satisfied [45].

$$a_B n^{\frac{1}{3}} \approx 0.25 \tag{5}$$

Here, a_B is Bohr radius and n is the critical carrier concentration. The critical carrier concentration in doped-$SrTiO_3$, has been reported to be on the order of $10^{18}\ cm^{-3}$ [46]. The carrier concentration on the order of $10^{20}\ cm^{-3}$ estimated for STN + G composites suggests that these materials have satisfied the Mott criteria. However, in spite of satisfying the Mott criteria these composites exhibit semiconductor-like behavior near room temperature, which can be explained by the Anderson transition [47–49]. Anderson transition has been found in the perovskite oxides [50–55], where charge carriers are localized due to local strain and variable electric field. The occurrence of point defects due to the multivalent cations (Ti^{4+}/Ti^{3+} and Nb^{5+}/Nb^{4+}) in STN is expected to create a large variation in local electric field and lattice distortion around these defect centers, which causes localization of itinerant

electrons in these oxides, known as Anderson's localization. Hence, STN has not been found to exhibit metal-like ($d\sigma/dT < 0$) behavior in the electrical conductivity vs. temperature plot unlike the Seebeck coefficient values, which follows the degenerate Fermi-gas model. Instead, charge carriers face an activation energy barrier in STN, which has been overcome at high-temperature resulting in S-M transitions. As the temperature increases, localized electrons are excited to itinerant state above mobility edge and display the metallic behavior. That might be the reason why thermally-activated weighted mobility has been observed in low-temperature regime (Fig. 3(e)). Furthermore, the charge carriers in all STN + G samples have been found to follow small-polaron hopping (SPH) model of conduction in the semiconductor region (below S-M transition temperature) as shown in Fig. 3(f). SPH conduction mechanism has been observed by many researchers for complex oxides [56,57]. The electrical conductivity governed by SPH [58,59] is given by,

$$\sigma = \frac{\sigma_0}{T}\exp\left[-\frac{E_{Hop}}{k_B T}\right] \tag{6}$$

Where σ_0 is constant, E_{Hop} is activation energy of small-polaron hopping, K_B is Boltzmann constant and T is absolute temperature. The activation energy (E_{Hop}) values have been found to decrease with loading graphite in the composite, indicating a general ease to the conduction process as shown in Table S7. However, a decrease in activation energy alone can't be attributed for such a large increase in electrical conductivity. It is to be noted here that the cross-over temperature from thermally-activated weighted mobility to μ_w due to scattering by acoustic phonons has been found to shift towards a lower temperature as graphite is introduced in STN matrix (Fig. 3(e)), which is similar to the shift in $T_{S\text{-}M}$ found in the composites (Table S6 & Fig. S12). The interesting feature to be noted here is the correlation between the increase in σ_{max} values with the decrease in S-M transition temperature due to graphite incorporation in STN from 617 K for pure STN to 474 K for 1 wt% G composition. Here, we propose that the inclusions of conductive graphite in STN matrix indeed act as facilitator for the transport of electrons, which otherwise would have suffered from Anderson's localization [47–49] due to the inherent presence of multivalent cations and point defects in STN ceramics. The incorporation of graphite in STN matrix augurs the delocalization of Anderson-localized electrons in STN resulting in occurrence of more itinerant electrons with higher mobility, which in turns enables the composites to exhibit metallic behavior at lower temperature compared to pure STN sample. For the composition $x \geq 1.5$, although S-M transition temperature has been found to increase but remains below the transition temperature corresponding to pure STN with the σ_{max} values higher than that of pure STN. The shift in S-M transition temperature ($T_{S\text{-}M}$) can be explained by lattice strain in analogy with nickel-based perovskites. Stability of metallic states by lattice strain was previously reported in rare earth nickelates ($RNiO_3$) by various researchers [60–62]. Recently, we have shown that comparatively less-conducting graphene oxide can trigger the Anderson localized electrons to become itinerant giving rise the semiconductor to metal transition with 250 times surge in electrical conductivity compared to pure STN [63]. Presence of a graphitic network in the STN matrix is expected to create a strain field around STN grains, which can be attributed to the reason for the metallic behavior at lower temperature in STN+G composites.

Although further theoretical and experimental evidences are required to fully understand role of Anderson localization in the conductivity of these composites, we have posited here two plausible phenomena behind enhanced electrical conductivity. Firstly, it is believed that presence of graphite in STN matrix creates a strain field, which enables the localized electrons to become itinerant similar to what has been observed in nickelates. Secondly, it has been hypothesized that the formation of a 3D conducting pathway for electrons due to the presence of graphite inclusions in the matrix of a less conducting STN oxide enhances the energy of the transporting electrons, since electron transport inside graphite is expected to be much faster compared to the activated conduction in STN grains. As a result, conduction of high energy electrons through graphite grains may facilitate more electrons to acquire the itinerant state above the mobility edge in STN. Further, these delocalized electrons possessing higher mobility dominate the charge transport in the composites resulting in augmentation of electrical conductivity values. As shown schematically in Fig. 3(g), the presence of graphite with a wide distribution of sizes from nm-scale inclusions to micron-sized grains (similar in size of STN grains) has laid out not only a smoother conducting path for electrons as compared to electron hopping in pure STN grains, but also presence of high-energy electrons emerging from graphite facilitates a greater number of electrons to become delocalized in STN. So, the activation energy in these samples is believed to be dominated by mobility. Since the conductivity is dominated by the mobility enhancement due to delocalization of electrons which encounter Anderson's localization in STN, Seebeck coefficient has been found to remain unaffected due to graphite incorporation; because thermopower is inversely proportional to the electron concentrations whether they are localized or delocalized [64] and carrier concentration in all the compositions remain unaltered.

The thermal analysis, as shown in Fig. 4(a), implies a mutual cancellation of the two contributors (κ_l and κ_e) resulting in the κ values for all the composites to remain in the same band of data points with increase in graphite loading. This is interesting from the fact that in spite of significant increase in κ_e (Fig. S13(d)) due to the large enhancement of σ with graphite loading, we have been able to limit the increase in total thermal conductivity, because κ_l has decreased significantly in the high temperature region due to the graphite addition (Fig. 4(b)). Earlier researchers [15–17,38] have also reported ~25% decrease in κ_l in doped-$SrTiO_3$ by making the composites with graphene as shown in Table S5. It is apparent that graphite inclusions distributed in STN matrix have caused enhanced phonon scattering at the matrix-inclusion interface as shown schematically in Fig. 3(g).

Furthermore, we have calculated the variation of phonon mean-free path (L_{phonon}) using the Eq. (7) in the whole temperature range of measurement for all the compositions as shown in Fig. 4(c) [64].

$$L_{phonon} = \frac{3\kappa_l}{C_v . \upsilon_m} \tag{7}$$

C_v and υ_m are isochoric heat capacity and the mean velocity of sound in the material respectively. υ_m has been calculated by the bulk modulus and shear modulus obtained from nanoindentation test as explained in the Supporting Information along with their estimated values presented in Table S8. The calculated values of L_{phonon} for STN+G composites have been found to be smaller than the earlier reports on $SrTiO_3$-based oxides [65,66] and composites;[38] introduction of graphite in STN matrix decreases its L_{phonon}. Remarkably, L_{phonon} of all the graphite-containing composites has been found to be constant above 700 K, which is very close to the Debye temperature (θ_D) calculated for all the compositions from sound velocity as shown in Table S8. Such constant mean-free path behavior with variation of temperature is generally observed in phonon glass system [67,68] suggesting the localization of vibration in the composites of STN matrix with graphite inclusions.

In order to understand the role of various phonon scattering processes occurring in the STN+G composites system, lattice thermal conductivity (κ_l) has been further analysed by Callaway's model [69] expressed as

$$\kappa_l = \frac{k_B}{2\pi^2 v}\left(\frac{k_B T}{\hbar}\right)^3 \int_0^{\theta_D/T} \frac{\tau(y,T) y^4 e^y}{(e^y-1)^2} dy \tag{8}$$

where, $y = \hbar\omega/k_B T$, ω is phonon frequency, ħ is reduced Plank's constant, θ_D is Debye temperature, v_m is mean acoustic velocity and τ is relaxation time expressed by Eq. (10), which is the sum of grain boundary scattering (τ_B), point defect scattering (τ_{PD}), phonon-phonon

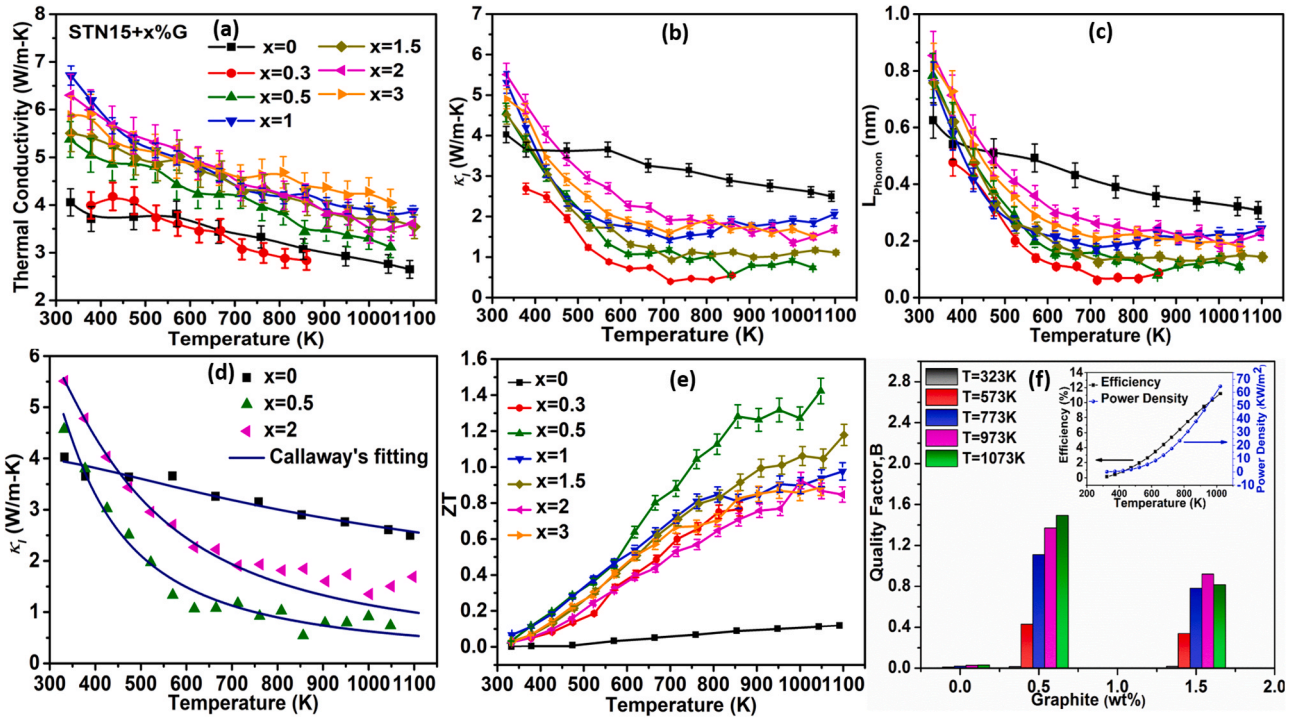

Fig. 4. Thermal properties and Power output analysis, Plot of (a) Thermal Conductivity with Temperature (b) κ_l with Temperature (c) Mean free path of phonon (L_{Phonon}) with temperature (d) Debye Callaway model fitting (Violet line) of experimentally determined lattice thermal conductivities (κ_l) for Pure and composite samples with different wt% (x) of graphite (e) ZT with Temperature for sintered STN+x wt% G composites ($0 \leq x \leq 3$) (f) Quality Factor (B) with an inset of Efficiency and power output density plot as a function of hot end temperature while cold end was fixed at 300 K.

Umpklapp scattering (τ_U) and electron-phonon scattering ($\tau_{e\text{-}p}$) [70,71].

$$\tau^{-1} = \tau_B^{-1} + \tau_{PD}^{-1} + \tau_U^{-1} + \tau_{ep}^{-1} = \frac{v_m}{L} + A\omega^4 + B\omega^2 T e^{\frac{-\theta_D}{mT}} + C\omega^2 \quad (9)$$

Here, L is average grain size and A, B and C are the fitting parameters, related to point-defect scattering, the Umklapp (U) process and electron-phonon scattering, respectively. As suggested by Slack [72,73], value of m in Eq. (10) should be greater than 1. We have kept m = 1.2 to obtain the best fit. It is to be noted that the influence of normal processes has been neglected here. Since, the grain boundary scattering is observed only at very low temperatures as suggested by Casimir [74], it has been omitted here too. Furthermore, the contribution of point-defect scattering at room-temperature has been found to be less than 0.3% of the total thermal conductivity as calculated [75,76] from the thermal resistance shown in the Eq. (11)&(12).

$$R_l^{th} = R_{PD} + R_U + R_{ep} \quad (10)$$

Where, $R_l^{th} = \left(\frac{1}{\kappa_l}\right)$ is the lattice thermal resistivity and R_{PD}, R_U and R_{ep} are thermal resistance for point defect, Umklapp and electron-phonon scattering expressed as

$$R_{PD} = \frac{4\pi^2 V_o \theta_D \Gamma}{h v_m^2},\ R_U = \frac{\pi v_m h B T}{\theta_D {k_B}^2} \text{and} R_{ep} = \frac{\pi v_m h c}{\theta_D {k_B}^2} \quad (11)$$

where Γ is scattering parameter [73] and V_o is average volume per atom in the crystal. The Callaway model considering Umklapp and electron-phonon scattering has been found to fit well with the lattice thermal conductivity data of all the compositions as shown in Fig. 4(d). From the fitting parameters presented in Table S9, it is evident that Umklapp scattering factor B in the Callaway model increases by one order of magnitude in the STN + G composite system compared to that of pure STN. However, electron-phonon scattering parameter, C doesn't really change much due to graphite loading, although it increases slightly with increase in graphite concentration. Hence, the dominating Umklapp scattering has been attributed to be the reason behind decrease in κ_l of composite samples especially at high temperatures due to graphite incorporation. It is noteworthy that room-temperature values of κ_l for composite samples have been higher than that of pure STN. This can be explained from much steeper slope obtained in lattice thermal conductivity graph of composites near room temperature arising from the order-of-magnitude higher Umklapp scattering, overshadowing other scattering effects similar to what has been described by Slack [72].

Controlling the increasing rate of thermal conductivity by introducing enhanced phonon scattering in STN matrix by graphite inclusions, in spite of phenomenal increase in electrical conductivity has led us to realize 15-times increase in the ZT values in composites than pure STN as shown in Fig. 4(e). Highest ZT value of 1.42 has been achieved at ~ 1050 K for STN+ 0.5 wt%G composition. Importantly, this oxide composite has shown ZT > 1.2 in the broad temperature range, 850–1050 K which offers a broad operational thermal window, extremely desirable for practical application as TEG. Moreover, three different STN+G compositions have exhibited ZT > 1 without using any toxic and expensive rare-earth elements which has so far never been realized in any n-type oxide. Furthermore, dimensionless thermoelectric Quality factor (B) has been calculated from the Eq. (13) to estimate the effect of graphite in STN [77,78].

$$B = \left(\frac{k_B}{e}\right)^2 \frac{8\pi e (2 m_e k_B T)^{3/2}}{3h^3} \cdot \frac{\mu_w}{\kappa_l} T \quad (12)$$

Fig. 4(f)) displays the B values at different temperatures for varied graphite content (0,0.5,1.5), where x = 0.5 wt% exhibits a large scale increase in B value of 1.49 at 1073 K compared to pure STN and this value is comparable to many of the state-of-art thermoelectric material such as selenide or telluride-based materials [79–82]. This sharp increase in B value for the graphite composites can be attributed to augmentation in μ_w and reduction in κ_l value because of graphite incorporation in STN matrix as already mentioned earlier.

3.3. Efficiency calculation

In literature, maximum efficiency of any thermoelectric material has been calculated as[83].

$$\eta_{max} = \eta_c \frac{\sqrt{1+Z.T_{avg}}-1}{\sqrt{1+Z.T_{avg}}+\frac{T_c}{T_h}} \quad (13)$$

where, Z is figure-of-merit at average temperature, and T_c, T_h are cold and hot end temperatures, respectively. Calculation based on Eq. (14) has given a value of 15.7% efficiency for our STN + 0.5 wt% G composite. However, a more advanced formula for efficiency calculation based on cumulative material properties has been proposed by Kim *et. al* [84] as

$$\eta_{max} = \eta_c \frac{\sqrt{1+ZT_{eng}\left(\frac{\widehat{\alpha}}{\eta_c}-\frac{1}{2}\right)}-1}{\left(\sqrt{1+ZT_{eng}\left(\frac{\widehat{\alpha}}{\eta_c}-\frac{1}{2}\right)}+1\right)-\eta_c} \quad (14)$$

where, η_c is Carnot efficiency and ZT_{eng} is the engineering dimensionless figure of merit defined as =

$$(ZT)_{eng} = \frac{\left(\int_{T_c}^{T_h} S(T)dT\right)^2}{\int_{T_c}^{T_h}\rho(T)dT \int_{T_c}^{T_h} k(T)dT}\Delta T \quad (15)$$

and, $\widehat{\alpha}$ is a dimensionless intensity factor of the Thomson effect defined as

$$\widehat{\alpha} = \frac{S(T_h)\quad \Delta T}{\int_{T_c}^{T_h} S(T)dT} \quad (16)$$

Where, $S(T_h)$ denotes the value of Seebeck coefficient at hot temperature. Using Eq. (15), we have estimated maximum efficiency of 10.7% for our composite sample. Further, to evaluate the potential of STN + G composites for fabrication of TEG we have carried out finite element modeling (FEM) to determine their energy conversion efficiency. A 3D model of STN + 0.5 wt% G leg of dimensions 2 mm x 2 mm x 8 mm, with 0.2 mm thick platinum electrodes at both the hot and cold ends, has been created in COMSOL Multiphysics as described in details in Supporting Information. All the procedures in FEM such as leg construction, meshing and the output results such as temperature distribution, potential distribution and current density in the TE legs are shown in the Fig. S15. The power output density and efficiency obtained from finite element analysis of a single TE leg at varying hot end temperature are shown in the inset of Fig. 4(f). The single TE leg of STN+G composite has shown maximum efficiency of 11.2% with maximum power output density of 64.6 kW/m^2. The measured heat flux input has been found to be 0.57 MW/m^2 suggesting the capability of the present oxide composites of converting ~ MW level waste heat into ~kW level electricity.

4. Conclusion

In summary, the inclusions of graphite in the matrix of Nb-doped $SrTiO_3$ oxide have formed a smoother conduction pathway for electrons leading to 21-times increase in weighted mobility (μ_w) of electrons causing the surge in the electrical conductivity and large enhancement in TE power factor of STN + G composites. Furthermore, graphite inclusions have induced enhanced Umklapp scattering in the composites restricting the increase in thermal conductivity. As a result, record high ZT ~ 1.42 has been attained in STN + 0.5 wt% G oxide composite made of earth-abundant elements. Although these oxide-based composites have shown high figure-of-merit, it is necessary to measure the efficiency of multi-leg TEG in real waste-heat source condition in order to realize their wide-scale commercialization. Nevertheless, our results have provided a new and better recipe for designing high-performance oxide-based thermoelectric composites by selection of inexpensive natural graphite among various carbon-based materials, which can be further extended for state-of-the-art chalcogenides, intermetallics and other materials.

CRediT authorship contribution statement

T.M. was responsible for the original research concept and physical interpretation. M.A. synthesized the samples and performed the experiments. M.A. and S.S.J. analyzed the data with the help of T.M. M.R. carried out FEM simulations. M.A., S.S.J. and M.R. wrote the main manuscript with the help of T.M.

Declaration of Competing Interest

The authors declare that they have no known competing financial interests or personal relationships that could have appeared to influence the work reported in this paper.

Acknowledgement

This work is supported by the grant from Science and Engineering Research Board, Department of Science and Technology (SERB-DST), India (Grant No: IMP/20l8/000955).

Appendix A. Supporting information

Supplementary data associated with this article can be found in the online version at doi:10.1016/j.nanoen.2021.105905.

References

[1] A. Firth, B. Zhang, A. Yang, Quantification of global waste heat and its environmental effects, Appl. Energy 235 (2019) 1314–1334.
[2] J. He, M.G. Kanatzidis, V.P. Dravid, High performance bulk thermoelectrics via a panoscopic approach, Mater. Today 16 (5) (2013) 166–176.
[3] Y. Liu, L.D. Zhao, Y. Zhu, Y. Liu, F. Li, M. Yu, D.B. Liu, W. Xu, Y.H. Lin, C.W. Nan, Synergistically optimizing electrical and thermal transport properties of BiCuSeO via a dual-doping approach, Adv. Energy Mater. 6 (9) (2016), 1502423.
[4] N. Van Nong, N. Pryds, S. Linderoth, M. Ohtaki, Enhancement of the thermoelectric performance of p-type layered oxide Ca3Co4O9+ δ through heavy doping and metallic nanoinclusions, Adv. Mater. 23 (21) (2011) 2484–2490.
[5] I. Terasaki, Y. Sasago, K. Uchinokura, Large thermoelectric power in NaCo2O4 single crystals, Phys. Rev. B 56 (20) (1997) R12685–R12687.
[6] K. Park, J.S. Son, S.I. Woo, K. Shin, M.-W. Oh, S.-D. Park, T. Hyeon, Colloidal synthesis and thermoelectric properties of La-doped SrTiO3 nanoparticles, J. Mater. Chem. A 2 (12) (2014) 4217–4224.
[7] S. Ohta, T. Nomura, H. Ohta, M. Hirano, H. Hosono, K. Koumoto, Large thermoelectric performance of heavily Nb-doped SrTiO3 epitaxial film at high temperature, Appl. Phys. Lett. 87 (9) (2005), 092108.
[8] J. Wang, B.-Y. Zhang, H.-J. Kang, Y. Li, X. Yaer, J.-F. Li, Q. Tan, S. Zhang, G.-H. Fan, C.-Y. Liu, Record high thermoelectric performance in bulk SrTiO3 via nano-scale modulation doping, Nano Energy 35 (2017) 387–395.
[9] B. Zhang, J. Wang, T. Zou, S. Zhang, X. Yaer, N. Ding, C. Liu, L. Miao, Y. Li, Y. Wu, High thermoelectric performance of Nb-doped SrTiO3 bulk materials with different doping levels, J. Mater. Chem. C 3 (43) (2015) 11406–11411.
[10] A.V. Kovalevsky, M.H. Aguirre, S. Populoh, S.G. Patrício, N.M. Ferreira, S. M. Mikhalev, D.P. Fagg, A. Weidenkaff, J.R. Frade, Designing strontium titanate-based thermoelectrics: insight into defect chemistry mechanisms, J. Mater. Chem. A 5 (8) (2017) 3909–3922.
[11] A. Tkach, Jo Resende, K.V. Saravanan, M.E. Costa, P. Diaz-Chao, E. Guilmeau, O. Okhay, P.M. Vilarinho, Abnormal grain growth as a method to enhance the thermoelectric performance of Nb-doped strontium titanate ceramics, ACS Sustain. Chem. Eng. 6 (12) (2018) 15988–15994.
[12] B. Feng, J. Xie, G. Cao, T. Zhu, X. Zhao, Enhanced thermoelectric properties of p-type CoSb 3/graphene nanocomposite, J. Mater. Chem. A 1 (42) (2013) 13111–13119.
[13] H. Chen, C. Yang, H. Liu, G. Zhang, D. Wan, F. Huang, Thermoelectric properties of CuInTe 2/graphene composites, CrystEngComm 15 (34) (2013) 6648–6651.
[14] J. Dong, W. Liu, H. Li, X. Su, X. Tang, C. Uher, In situ synthesis and thermoelectric properties of PbTe–graphene nanocomposites by utilizing a facile and novel wet chemical method, J. Mater. Chem. A 1 (40) (2013) 12503–12511.
[15] Y. Lin, C. Norman, D. Srivastava, F. Azough, L. Wang, M. Robbins, K. Simpson, R. Freer, I.A. Kinloch, Thermoelectric power generation from lanthanum strontium titanium oxide at room temperature through the addition of graphene, ACS Appl. Mater. Interfaces 7 (29) (2015) 15898–15908.

[16] C. Wu, J. Li, Y. Fan, J. Xing, H. Gu, Z. Zhou, X. Lu, Q. Zhang, L. Wang, W. Jiang, The effect of reduced graphene oxide on microstructure and thermoelectric properties of Nb-doped A-site-deficient SrTiO3 ceramics, J. Alloy. Compd. 786 (2019) 884–893.

[17] O. Okhay, S. Zlotnik, W. Xie, K. Orlinski, M.J.H. Gallo, G. Otero-Irurueta, A. J. Fernandes, D.A. Pawlak, A. Weidenkaff, A. Tkach, Thermoelectric performance of Nb-doped SrTiO3 enhanced by reduced graphene oxide and Sr deficiency cooperation, Carbon 143 (2019) 215–222.

[18] L. Ferrer-Argemi, Z. Yu, J. Kim, N.V. Myung, J.-H. Lim, J. Lee, Silver content dependent thermal conductivity and thermoelectric properties of electrodeposited antimony telluride thin films, Sci. Rep. 9 (1) (2019) 1–8.

[19] D. Pinisetty, R. Devireddy, Thermal conductivity of semiconductor (bismuth–telluride)–semimetal (antimony) superlattice nanostructures, Acta Mater. 58 (2) (2010) 570–576.

[20] A. Alofi, G. Srivastava, Thermal conductivity of graphene and graphite, Phys. Rev. B 87 (11) (2013), 115421.

[21] J.U. Rahman, N. Van Du, W.H. Nam, W.H. Shin, K.H. Lee, W.-S. Seo, M.H. Kim, S. Lee, Grain boundary interfaces controlled by reduced graphene oxide in nonstoichiometric SrTiO 3-δ thermoelectrics, Sci. Rep. 9 (1) (2019) 1–12.

[22] P. Roy, V. Waghmare, T. Maiti, Environmentally friendly Ba x Sr 2− x TiFeO 6 double perovskite with enhanced thermopower for high temperature thermoelectric power generation, RSC Adv. 6 (60) (2016) 54636–54643.

[23] Z. Marković, M. Budimir, D. Kepić, I. Holclajtner-Antunović, M. Marinović-Cincović, M. Dramićanin, V. Spasojević, D. Peruško, Z. Špitalský, M. Mičušik, Semi-transparent, conductive thin films of electrochemical exfoliated graphene, RSC Adv. 6 (45) (2016) 39275–39283.

[24] S. Balasubramanyan, S. Sasidharan, R. Poovathinthodiyil, R.M. Ramakrishnan, B. N. Narayanan, Sucrose-mediated mechanical exfoliation of graphite: a green method for the large scale production of graphene and its application in catalytic reduction of 4-nitrophenol, N. J. Chem. 41 (20) (2017) 11969–11978.

[25] H.J. Kim, S.-M. Lee, Y.-S. Oh, Y.-H. Yang, Y.S. Lim, D.H. Yoon, C. Lee, J.-Y. Kim, R. S. Ruoff, Unoxidized graphene/alumina nanocomposite: fracture-and wear-resistance effects of graphene on alumina matrix, Sci. Rep. 4 (2014) 5176.

[26] K. Koumoto, Y. Wang, R. Zhang, A. Kosuga, R. Funahashi, Oxide thermoelectric materials: a nanostructuring approach, Annu. Rev. Mater. Res. 40 (2010) 363–394.

[27] P. Roy, V. Pal, T. Maiti, Effect of Spark Plasma Sintering (SPS) on the thermoelectric properties of SrTiO3: 15 at% Nb, Ceram. Int. 43 (15) (2017) 12809–12813.

[28] H. Wang, W. Su, J. Liu, C. Wang, Recent development of n-type perovskite thermoelectrics, J. Mater. 2 (3) (2016) 225–236.

[29] T. Teranishi, Y. Ishikawa, H. Hayashi, A. Kishimoto, M. Katayama, Y. Inada, Thermoelectric efficiency of reduced SrTiO 3 ceramics modified with La and Nb, J. Am. Ceram. Soc. 96 (9) (2013) 2852–2856.

[30] D. Ekren, F. Azough, A. Gholinia, S.J. Day, D. Hernandez-Maldonado, D. M. Kepaptsoglou, Q.M. Ramasse, R. Freer, Enhancing the thermoelectric power factor of Sr 0.9 Nd 0.1 TiO 3 through control of the nanostructure and microstructure, J. Mater. Chem. A 6 (48) (2018) 24928–24939.

[31] S. Ohta, T. Nomura, H. Ohta, K. Koumoto, High-temperature carrier transport and thermoelectric properties of heavily La-or Nb-doped Sr Ti O3 single crystals, J. Appl. Phys. 97 (3) (2005), 034106.

[32] N. Wang, H. He, Y. Ba, C. Wan, K. Koumoto, Thermoelectric properties of Nb-doped SrTiO3 ceramics enhanced by potassium titanate nanowires addition, J. Ceram. Soc. Jpn. 118 (1383) (2010) 1098–1101.

[33] Y. Lin, M.T. Dylla, J.J. Kuo, J.P. Male, I.A. Kinloch, R. Freer, G.J. Snyder, Graphene/strontium titanate: approaching single crystal–like charge transport in polycrystalline oxide perovskite nanocomposites through grain boundary engineering, Adv. Funct. Mater. 30 (12) (2020), 1910079.

[34] G.J. Snyder, A.H. Snyder, M. Wood, R. Gurunathan, B.H. Snyder, C. Niu, Weighted mobility, Adv. Mater. 32 (2020), 2001537.

[35] R. Chasmar, R. Stratton, The thermoelectric figure of merit and its relation to thermoelectric generators, Int. J. Electron. 7 (1) (1959) 52–72.

[36] H.J. Goldsmid, Thermoelectric refrigeration, (1964).

[37] G.A. Slack, D. Rowe, CRC handbook of thermoelectrics, CRC press, Boca Raton, FL, 1995.

[38] N. Wang, H. Chen, H. He, W. Norimatsu, M. Kusunoki, K. Koumoto, Enhanced thermoelectric performance of Nb-doped SrTiO3 by nano-inclusion with low thermal conductivity, Sci. Rep. 3 (2013) 3449.

[39] J.U. Rahman, N. Van Du, W.H. Nam, W.H. Shin, K.H. Lee, W.-S. Seo, M.H. Kim, S. Lee, Grain boundary interfaces controlled by reduced graphene oxide in nonstoichiometric SrTiO 3-δ thermoelectrics, Sci. Rep. 9 (1) (2019) 8624.

[40] M.T. Dylla, J.J. Kuo, I. Witting, G.J. Snyder, Grain boundary engineering nanostructured SrTiO3 for thermoelectric applications, Adv. Mater. Interfaces 6 (15) (2019), 1900222.

[41] L. Bjaalie, A. Janotti, B. Himmetoglu, C. Van de Walle, Turning SrTiO3 into a Mott insulator, Phys. Rev. B 90 (19) (2014), 195117.

[42] T. Okuda, K. Nakanishi, S. Miyasaka, Y. Tokura, Large thermoelectric response of metallic perovskites:Sr1−xLaxTiO3 (0<˜ x<˜ 0. 1), Phys. Rev. B 63 (11) (2001), 113104.

[43] W. Wunderlich, H. Ohta, K. Koumoto, Enhanced effective mass in doped SrTiO3 and related perovskites, Phys. B: Condens. Matter 404 (16) (2009) 2202–2212.

[44] C. Lee, J. Destry, J. Brebner, Optical absorption and transport in semiconducting SrTiO3, Phys. Rev. B 11 (6) (1975) 2299–2310.

[45] N.F. Mott, The basis of the electron theory of metals, with special reference to the transition metals, Proceedings of the Physical Society. Section A 62(7) 1949 416.

[46] P.A. Cox, Transition metal oxides: an introduction to their electronic structure and properties, Oxford university press, 2010.

[47] P.W. Anderson, Absence of diffusion in certain random lattices, Phys. Rev. 109 (5) (1958) 1492–1505.

[48] P. Bernasconi, I. Biaggio, M. Zgonik, P. Günter, Anisotropy of the electron and hole drift mobility in KNbO 3 and BaTiO 3, Phys. Rev. Lett. 78 (1) (1997) 106–109.

[49] H. Ihrig, D. Hennings, Electrical transport properties of n-type BaTi O 3, Phys. Rev. B 17 (12) (1978) 4593–4599.

[50] A. Biswas, K.-S. Kim, Y.H. Jeong, Metal insulator transitions in perovskite SrIrO3 thin films, J. Appl. Phys. 116 (21) (2014), 213704.

[51] S. Gilbert, L. Wills, B.W. Wessels, J. Schindler, J. Thomas, C. Kannewurf, Electrical transport properties of epitaxial BaTiO3 thin films, J. Appl. Phys. 80 (2) (1996) 969–977.

[52] Y. Li, J. Liu, J.-C. Li, Y.-F. Chen, X.-M. Zhang, X.-J. Wang, F.-N. Wang, W.-B. Su, L.-L. Zhao, C.-L. Wang, Electron localization in niobium doped CaMnO 3 due to the energy difference of electronic states of Mn and Nb, Phys. Chem. Chem. Phys. 20 (31) (2018) 20571–20574.

[53] S. Lee, J.A. Bock, S. Trolier-McKinstry, C.A. Randall, Ferroelectric-thermoelectricity and Mott transition of ferroelectric oxides with high electronic conductivity, J. Eur. Ceram. Soc. 32 (16) (2012) 3971–3988.

[54] T. Maiti, M. Saxena, P. Roy, Double perovskite (Sr 2 B′ B ″O 6) oxides for high-temperature thermoelectric power generation—A review, J. Mater. Res. (2018) 1–19.

[55] P. Roy, V. Waghmare, K. Tanwar, T. Maiti, Large change in thermopower with temperature driven p–n type conduction switching in environment friendly Ba x Sr 2− x Ti 0.8 Fe 0.8 Nb 0.4 O 6 double perovskites, Phys. Chem. Chem. Phys. 19 (8) (2017) 5818–5829.

[56] J.A. Bock, S. Trolier-McKinstry, G.D. Mahan, C.A. Randall, Polarization-based perturbations to thermopower and electronic conductivity in highly conductive tungsten bronze structured (Sr, Ba) Nb 2 O 6: Relaxors vs normal ferroelectrics, Phys. Rev. B 90 (11) (2014), 115106.

[57] M. Schrade, R. Kabir, S. Li, T. Norby, T. Finstad, High temperature transport properties of thermoelectric CaMnO3− δ—Indication of strongly interacting small polarons, J. Appl. Phys. 115 (10) (2014), 103705.

[58] T. Holstein, Studies of polaron motion: Part II. The “small” polaron, Ann. Phys. 8 (3) (1959) 343–389.

[59] R. Raffaelle, H.U. Anderson, D.M. Sparlin, P.E. Parris, Transport anomalies in the high-temperature hopping conductivity and thermopower of Sr-doped La (Cr, Mn) O 3, Phys. Rev. B 43 (10) (1991) 7991–7999.

[60] Y. Kumar, R. Choudhary, S. Sharma, M. Knobel, R. Kumar, Strain dependent stabilization of metallic paramagnetic state in epitaxial NdNiO3 thin films, Appl. Phys. Lett. 101 (13) (2012), 132101.

[61] J. Liu, M. Kareev, D. Meyers, B. Gray, P. Ryan, J. Freeland, J. Chakhalian, Metal-insulator transition and orbital reconstruction in Mott-type quantum wells made of NdNiO 3, Phys. Rev. Lett. 109 (10) (2012), 107402.

[62] N. Palina, L. Wang, S. Dash, X. Yu, M.B. Breese, J. Wang, A. Rusydi, Investigation of the metal–insulator transition in NdNiO 3 films by site-selective X-ray absorption spectroscopy, Nanoscale 9 (18) (2017) 6094–6102.

[63] P. Dey, S.S. Jana, F. Anjum, T. Bhattacharya, T. Maiti, Effect of semiconductor to metal transition on thermoelectric performance in oxide nanocomposites of SrTi0. 85Nb0. 15O3 with graphene oxide, Appl. Mater. Today 21 (2020), 100869.

[64] C. Kittel, P. McEuen, P. McEuen, Introduction to Solid State Physics, Wiley New York, 1996.

[65] Y. Wang, K. Fujinami, R. Zhang, C. Wan, N. Wang, Y. Ba, K. Koumoto, Interfacial thermal resistance and thermal conductivity in nanograined SrTiO3, Appl. Phys. Express 3 (3) (2010), 031101.

[66] S. Bhattacharya, A. Mehdizadeh Dehkordi, S. Tennakoon, R. Adebisi, J. Gladden, T. Darroudi, H.N. Alshareef, T. Tritt, Role of phonon scattering by elastic strain field in thermoelectric Sr1− xYxTiO3− δ, J. Appl. Phys. 115 (22) (2014), 223712.

[67] M.D. Nielsen, V. Ozolins, J.P. Heremans, Lone pair electrons minimize lattice thermal conductivity, Energy Environ. Sci. 6 (2) (2013) 570–578.

[68] D.G. Cahill, R.O. Pohl, Lattice vibrations and heat transport in crystals and glasses, Annu. Rev. Phys. Chem. 39 (1) (1988) 93–121.

[69] J. Callaway, Model for lattice thermal conductivity at low temperatures, Phys. Rev. 113 (4) (1959) 1046–1051.

[70] E. Langenberg, E. Ferreiro-Vila, V. Leborán, A. Fumega, V. Pardo, F. Rivadulla, Analysis of the temperature dependence of the thermal conductivity of insulating single crystal oxides, APL Mater. 4 (10) (2016), 104815.

[71] L. Daniels, S. Savvin, M. Pitcher, M. Dyer, J. Claridge, S. Ling, B. Slater, F. Cora, J. Alaria, M. Rosseinsky, Phonon-glass electron-crystal behaviour by A site disorder in n-type thermoelectric oxides, Energy Environ. Sci. 10 (9) (2017) 1917–1922.

[72] G.A. Slack, S. Galginaitis, Thermal conductivity and phonon scattering by magnetic impurities in CdTe, Phys. Rev. 133 (1A) (1964) A253–A268.

[73] G.A. Slack, Thermal conductivity of CaF2, MnF2, CoF2, and ZnF2, Phys. Rev. 122 (5) (1961) 1451–1464.

[74] H. Casimir, Note on the conduction of heat in crystals, Physica 5 (6) (1938) 495–500.

[75] V. Ambegaokar, Thermal resistance due to isotopes at high temperatures, Phys. Rev. 114 (2) (1959) 488–489.

[76] X. Shi, Y. Pei, G.J. Snyder, L. Chen, Optimized thermoelectric properties of Mo 3 Sb 7− x Te x with significant phonon scattering by electrons, Energy Environ. Sci. 4 (10) (2011) 4086–4095.

[77] A. Zevalkink, D.M. Smiadak, J.L. Blackburn, A.J. Ferguson, M.L. Chabinyc, O. Delaire, J. Wang, K. Kovnir, J. Martin, L.T. Schelhas, A practical field guide to thermoelectrics: fundamentals, Appl. Phys. Rev. 5 (2) (2018), 021303.

[78] Y. Pei, H. Wang, G.J. Snyder, Band engineering of thermoelectric materials, Adv. Mater. 24 (46) (2012) 6125–6135.

[79] I.T. Witting, T.C. Chasapis, F. Ricci, M. Peters, N.A. Heinz, G. Hautier, G.J. Snyder, The thermoelectric properties of bismuth telluride, Adv. Electron. Mater. 5 (6) (2019), 1800904.
[80] I.T. Witting, J.A. Grovogui, V.P. Dravid, G.J. Snyder, Thermoelectric transport enhancement of Te-rich bismuth antimony telluride (Bi0. 5Sb1. 5Te3+ x) through controlled porosity, J. Mater. 6 (2020) 532–544.
[81] Z. Geng, D. Shi, L. Shi, Y. Li, G.J. Snyder, K.-h Lam, Conventional sintered Cu2-xSe thermoelectric material, J. Mater. 5 (4) (2019) 626–633.
[82] P. Jood, J. Male, S. Anand, Y. Matsushita, Y. Takagiwa, M.G. Kanatzidis, G. J. Snyder, M. Ohta, Na doping in PbTe-solubility, band convergence, phase boundary mapping, and thermoelectric properties, J. Am. Chem. Soc. (2020).
[83] A. Ioffe, Semiconductor Thermoelements, and Thermoelectric, Cool-ingInfosearch Ltd., London, UK, 1957.
[84] H.S. Kim, W. Liu, G. Chen, C.-W. Chu, Z. Ren, Relationship between thermoelectric figure of merit and energy conversion efficiency, Proceedings of the National Academy of Sciences 112(27) 2015 8205–8210.
[85] M. Ohtaki, K. Araki, K. Yamamoto, High thermoelectric performance of dually doped ZnO ceramics, J. Electron. Mater. 38 (7) (2009) 1234–1238.
[86] A.A. Yaremchenko, S. Populoh, S.G. Patricio, J. Macias, P. Thiel, D.P. Fagg, A. Weidenkaff, J.R. Frade, A.V. Kovalevsky, Boosting thermoelectric performance by controlled defect chemistry engineering in Ta-substituted strontium titanate, Chem. Mater. 27 (14) (2015) 4995–5006.
[87] L. Bocher, M. Aguirre, D. Logvinovich, A. Shkabko, R. Robert, M. Trottmann, A. Weidenkaff, CaMn1− x Nb x O3 (x≤ 0.08) perovskite-type phases as promising new high-temperature n-type thermoelectric materials, Inorg. Chem. 47 (18) (2008) 8077–8085.

Megha Acharya is currently a doctoral student in Department of Materials Science and Engineering, University of California, Berkeley. She received Master's degree in Materials Science and Engineering from Indian Institute of Technology, Kanpur in 2018. Her research interests are focused on oxide-based electronic materials for multifunctional applications.

Subhra Sourav Jana is a Ph.D. scholar in Department of Materials Science and Engineering at Indian Institute of Technology, Kanpur. He received his B.Tech. and M.Tech degree in Ceramic Engineering from National Institute of Technology, Rourkela. He is recipient of prestigious "Prime Minister Research Fellow" scheme. His current research focus is the development of high performance oxide thermoelectrics for high temperature power generation from waste heat energy. His research interest also includes dielectric material, high entropy oxides, relaxor ferroelectrics.

Mani Ranjan received his Master's Degree in Materials Science & Engineering from IIT Kanpur in 2019. His Master's thesis was on 'Numerical Simulation and Performance optimization of Thermoelectric Generators'. He is currently working as a Researcher at Tata Steel R&D, Jamshedpur. His research interests are in the area of Thermoelectric materials, TEG converters, FEM, optimization techniques, Steel Making & Casting, Process Modelling, Energy Conservation and CO2 reduction.

Tanmoy Maiti is an Associate Professor and PK Kelkar Young Faculty Research Fellow in Department of Material Science and Engineering at IIT Kanpur, India. He received his Ph.D. degree from Pennsylvania State University. He earned his Masters in Ceramic Engineering from IIT-BHU and Bachelors in Ceramic Technology from College of Ceramic Technology, University of Calcutta. He did his post-doctoral research in Lawrence Berkeley National Laboratory and PennState University. His research interests span the areas of Thermoelectrics, Plasmonics, Photovoltaics and Oxide electronics. However, a common thread in his research is to address the global energy problem and designing next-generation chip-scale technology.